Yang *et al. Energy Mater.* **2025**, *5*, 500011
DOI: 10.20517/energymater.2024.83

Energy Materials

Article

A potential hydrogen isotope storage material Zr_2Fe: deep exploration on phase transition behaviors and disproportionation mechanism

Zhiyi Yang[1,#], Yuxiao Jia[1,#], Yang Liu[1], Xuezhang Xiao[1,*], Tiao Ying[1], Xingwen Feng[3,*], Yan Shi[3], Changan Chen[3], Wenhua Luo[3], Lixin Chen[1,2,*]

[1]State Key Laboratory of Silicon and Advanced Semiconductor Materials, School of Materials Science and Engineering, Zhejiang University, Hangzhou 310058, Zhejiang, China.
[2]Key Laboratory of Hydrogen Storage and Transportation Technology of Zhejiang Province, Hangzhou 310027, Zhejiang, China.
[3]Institute of Materials, China Academy of Engineering Physics, Mianyang 621700, Sichuan, China.
[#]The authors contributed equally to this work.

Correspondence to: Prof./Dr. Lixin Chen, State Key Laboratory of Silicon and Advanced Semiconductor Materials, School of Materials Science and Engineering, Zhejiang University, 866 Yuhangtang Rd., Hangzhou 310058, Zhejiang, China. E-mail: lxchen@zju.edu.cn; Dr. Xuezhang Xiao, State Key Laboratory of Silicon and Advanced Semiconductor Materials, School of Materials Science and Engineering, Zhejiang University, 866 Yuhangtang Rd., Hangzhou 310058, Zhejiang, China. E-mail: xzxiao@zju.edu.cn; Dr. Xingwen Feng, Institute of Materials, China Academy of Engineering Physics, 9 Huafeng New Village, Mianyang 621700, Sichuan, China. E-mail: fengxingwen@caep.cn

How to cite this article: Yang, Z.; Jia, Y.; Liu, Y.; Xiao, X.; Ying, T.; Feng, X.; Shi, Y.; Chen, C.; Luo, W.; Chen, L. A potential hydrogen isotope storage material Zr_2Fe: deep exploration on phase transition behaviors and disproportionation mechanism. *Energy Mater.* **2025**, *5*, 500011. https://dx.doi.org/10.20517/energymater.2024.83

Received: 19 Jul 2024 **First Decision:** 4 Nov 2024 **Revised:** 18 Nov 2024 **Accepted:** 27 Nov 2024 **Published:** 8 Jan 2025

Academic Editor: Sining Yun **Copy Editor:** Ping Zhang **Production Editor:** Ping Zhang

Abstract

Tritium, a radioactive isotope of hydrogen, is exceptionally rare and valuable. The safe storage, controlled release and efficient capture of tritium are subject to focused research in the International Thermonuclear Experimental Reactor. However, the application of an efficient tritium-getter material remains a critical challenge. Zr_2Fe alloys exhibit a strong ability to absorb low-concentration hydrogen isotopes, but their practicability suffers from disproportionation reaction. Yet, the essential de-/hydrogenation performances and disproportionation mechanism of Zr_2Fe are inconclusive. Here, we designed a comprehensive series of measurements that demonstrate the ultra-low hydrogenation equilibrium pressure (2.68×10^{-8} Pa at 25 °C) and unique hydrogen-interacted phase transitions in Zr_2Fe-H systems. Further kinetic and thermodynamic analyses reveal the causative reasons for disproportionation and determine the triggering temperature of the disproportionation reaction to be 375 °C in static hydrogen environments. Utilizing inversion of the Van't Hoff equation, higher-temperature hydrogen absorption models of Zr_2Fe are developed, supporting a solution to the inaccuracy and inseparability of the general de-/hydrogenation and disproportionation, thereby verifying the unique disproportionation route ($Zr_2Fe/Zr_2FeH_x + H_2 \rightarrow ZrFe_2 + ZrH_2$). Combined with the density functional theory (DFT) calculations, the de-/hydrogenation and disproportionation mechanisms and their interrelation can be explained in depth. This work supports the exploration and modification of the Zr_2Fe-H and other metal hydride storage systems in future studies.

Keywords: Tritium-getter materials, Zr_2Fe alloy, phase transition, disproportionation mechanism, DFT calculations

INTRODUCTION

In recent decades, the energy demands for social development have steadily risen, while excessive provision and utilization of fossil energy have caused the energy crisis and presented adverse effects on environmental harmony. Nuclear energy generated by a controllable nuclear fusion reaction (deuterium and tritium plasma) in the International Thermonuclear Experimental Reactor (ITER) is recognized as one of the most desirable sustainable energy systems owing to its environment-friendliness, low cost, safety, substantial energy release and fuel abundance[1,2]. The retention of tritium is an essential issue during recovery and storage due to its radioactivity and rarity. Meanwhile, a crucial security concern is to ensure the absence of tritium leakage. Consequently, it is imperative to collect tritium in the exhaust gas and equipment space. Tritium-getter materials should exhibit excellent hydrogen absorption kinetics and ultra-low equilibrium hydrogenation pressure to ensure high absorption efficiency. Thus, hydrogen storage alloys (HSAs) are attracting widespread interest in the nuclear industry, owing to their ability to capture hydrogen isotopes and generate stable metal hydrides.

At present, metallic Pd, depleted U and ZrCo-based alloys are available in hydrogen isotope separation/purification and storage/delivery systems. Pd is the first-discovered HSA and exhibits a significant isotope effect. The hydrogenated product of Pd is $PdH_{0.6}$ with a theoretical capacity of 0.565 wt%, and the hydrogenation equilibrium pressure under room temperature of Pd is about 2,700 Pa[3]. U-based alloys have rapid hydrogenation rates and relatively high rechargeable hydrogen storage capacities (~0.9 wt%) and reach low hydrogenation equilibrium pressures (10^{-3}~10^{-4} Pa at room temperature), but radioactivity is a challenge for U[4]. Compared to the Pd and U, ZrCo-based alloys are non-radioactive and low cost, having a high theoretical hydrogen storage capacity of 2 wt%, and a relatively low equilibrium pressure (~10^{-3} Pa at room temperature)[5]. Therefore, Zr-based alloys, especially those with high hydrogen-affinity Zr content, are of great interest in Tokamak exhaust processing (TEP) systems[6-9]. The Zr-rich alloys were once regarded as potential tritium absorption materials for capturing low-concentration tritium due to their high hydrogen storage capacity, rapid hydriding kinetics and much lower hydrogenation equilibrium pressure. Furthermore, their comprehensive evaluation requires consideration of indicators such as disproportionation resistance[10].

Hydrogen isotopes have similar physical and chemical properties, so hydrogen is usually used instead of tritium in the study of hydrogen isotope storage metals[11]. Early, the hydrogen absorption and disproportionation behaviors of Zr_2M (M = Ni, Co, Fe) alloys were reported and discussed in a summarized manner[12]. The room-temperature hydrogenation equilibrium pressure of Zr_2Ni alloys is reported to be approximately 500 Pa, which is too high for hydrogen isotope storage applications. Meanwhile, Zr_2Ni can be rapidly disproportionated into $ZrNiH_3$, ZrH_2 and a Zr-deficient compound (ZrNi) with the interaction of hydrogen at 500 °C; then, ZrNi reacts with H_2 to form disproportionation products ZrH_2 and Zr_7Ni_{10}[12,13]. Zr_2Co alloys have an ultra-low hydrogenation equilibrium pressure of 3.22×10^{-6} Pa at 25 °C, significantly lower than that of ZrCo alloys (10^{-3} Pa), and exhibit great hydriding kinetics at a low hydrogen pressure of

5,000 Pa due to their high content of hydrogen-affinity Zr[14]. However, Zr_2Co exhibits similar disproportionation behaviors to Zr_2Ni. During the elevated temperature dehydrogenation, the Zr_2CoH_5 hydride first decomposes into $ZrCoH_3$ and ZrH_2, making it highly susceptible to disproportionation. Although the disproportionation products can be reconstructed back to Zr_2Co at 800 °C, it is easy to induce tritium permeation and thermal radiation to the external environment during tritium recovery applications at such high reconstruction temperatures. Therefore, it is crucial to improve the anti-disproportionation properties of ultra-low hydrogen equilibrium pressure alloys at workable temperatures[15].

Regarding Zr_2Fe alloys, it was reported that Zr_2Fe beds can absorb the hydrogen isotopes to the concentration below the detection limit of gas chromatography (1 ppm) in a relatively short time, demonstrating excellent hydrogen absorption performance[16]. Importantly, its cyclic stability, i.e., the ability to resist disproportionation, is still a key consideration. Prigent *et al.*[17] investigated the cyclic performance of Zr_2Fe alloys under a hydrogen pressure of 1 bar, and the results demonstrated a sharp decay of hydrogen absorption capacity after cycling. Its initial hydrogenation capacity is about 1.88 wt%, following dehydrogenation at 350 °C for 3 h; the hydrogenation capacity decreases to only 0.84 wt% in the third cycle. Disproportionation products do not contribute to hydrogen storage capacity, directly indicating the disproportionation degree. Hara *et al.*[12] suggested that Zr_2Fe has peculiar behaviors of disproportionation that differ from Zr_2Ni and Zr_2Co, and exhibits relatively poorer stability to hydrogen-induced disproportionation. Song *et al.*[18] pointed out that Zr_2Fe would still be disproportionated even if hydrogenated at room temperature, and that the degree of disproportionation significantly intensified with initial hydrogen pressure. Nevertheless, Janot *et al.*[19] reported that only Zr_2FeH_5 and $Zr_3FeH_{6.7}$ phases were formed after hydrogen absorption in the Zr_2Fe and Zr_3Fe alloys. The phase transitions of Zr_2FeD_5 during the temperature-rise process were studied in situ by neutron diffraction; it was found that the disproportionation phase of ZrD_2 would not exist below 330 °C[20]. It follows that the disproportionation mechanism in the Zr_2Fe-H system remains controversial, and de-/hydrogenation performance has not been thoroughly investigated with comprehensive consideration of in-process control parameters. Simultaneously, the lack of consolidated understanding of the kinetic and thermodynamic properties, as well as the specific de-/hydrogenation performance indexes of Zr_2Fe, also hinders the exploration of disproportionation behaviors.

In this work, we have comprehensively studied the de-/hydrogenation properties in Zr_2Fe-H systems by precisely modulating hydrogen pressure, temperature and reactant loadings, and then investigated the variations of the corresponding crystal structures and phases. Subsequently, we progressively elicited and identified the practical triggering factors for the disproportionation reaction. The correlation between general de-/hydrogenation and disproportionation reactions was further examined in terms of kinetics and thermodynamics. Meanwhile, the reaction pathways of disproportionation reaction were defined. Finally, in conjunction with density functional theory (DFT) calculations in terms of energy variation and bonding strength, the mechanisms of general de-/hydrogenation and disproportionation in the Zr_2Fe-H system were deeply probed, and their competitive relationship in kinetics was further elucidated.

EXPERIMENTAL

Sample preparation

Zr_2Fe ingot was synthesized by induction levitation melting with high-purity metals in accordance with the stoichiometric ratio. The equipment used is a SPG-60AB high-frequency induction heater produced by Shenzhen Shuangping Power Supply Technologies Co. Ltd. The melting process of high-purity zirconium and iron (total weight of around 25 g) was performed in a water-cooled copper crucible under the protection of a 1.4 bar argon atmosphere (99.999%). The protection gas in the melting chamber was ensured by flushing with argon at room temperature. The ingot was turned over for re-melting three times to ensure high homogeneity. Stoichiometric amounts of high-purity zirconium (Zr, 99.9%) and iron (Fe, 99.9%) were supplied by the General Research Institute for Non-ferrous Metals.

Microstructure characterization

The morphology of the alloy was observed using a Hitachi SU-70 field-emission scanning electron microscope (FESEM). The elemental mapping was detected using an energy dispersive X-ray spectrometer (EDX) mounted on a scanning electron microscope (SEM). The phase structure was characterized by an X-ray diffractometer (XRD, Rigaku Ultima IV) with Cu-Kα radiation (λ = 0.154056 nm). The differential scanning calorimetry (DSC, Netzsch STA449F3) was detected in the Ar atmosphere.

Hydrogen storage performance measurements

A hydrogen storage performance test device (Sievert's type volumetric equipment) is made up of an electric furnace, a 10 ml stainless-steel reactor, two reservoirs with volumes of 100 ml and 750 ml, and three pressure sensors (test range: 0.01 - 160 bar, 0.001 - 10 bar and 0.1 - 1,024 Pa, respectively). High-purity hydrogen (99.999%) is adopted. In the initial activation process, crushed Zr_2Fe alloy powders were placed into a reactor and annealed at high temperatures under evacuation for a specific time, to get rid of the surface-adsorbed impurity gas. The activated samples were then used for subsequent experiments. The hydriding kinetics of activated samples were tested under the same initial hydrogen pressures (1 bar) at room temperature with different sample loadings of 0.25, 0.5 and 1.5 g. The Pressure-Composition-Temperature (PCT) measurements for de-/hydrogenation at different temperatures (325, 350, 375, 450, and 500 °C) were performed by progressively adjusting the hydrogen pressure in the reactor, with temperature fluctuations of less than 5 °C. The temperature-programmed dehydrogenation (TPD) experiments were performed with an initial hydrogen pressure of 10 Pa and a heating rate of 3 °C/min and 5 °C/min. Measurements involving disproportionation were conducted by designing parameters such as hydrogen pressure, temperature, reaction time, and the amount of hydrogen absorption. These parameters were systematically controlled to regulate the disproportionation reaction during de-/hydrogenation processes.

Apparent activation energy calculations

The hydrogenation fraction of a sample can be written as follows:

$$\alpha = (H_t - H_0)/(H_1 - H_0) \quad (1)$$

where α is the reaction fraction, and H_0, H_t and H_1 refer to the hydrogen capacity of a sample at begin, time t and final, respectively.

The rate of hydrogenation can be expressed by the following basic rate equation:

$$d\alpha/dt = k(T)f(\alpha) \quad (2)$$

where $f(\alpha)$ is a mathematical model that simulates the reaction, and the parameter $k(T)$ is the temperature-dependent reaction rate constant.

By integrating the above equation according to the method proposed by Sharp[21] and Jone[22], the reaction progress versus reaction time is obtained as follows:

$$g(\alpha) = k(T)t \tag{3}$$

Where $g(\alpha)$ represents the expression of a specific kinetic model. Different kinetic models each have a corresponding set of theoretical values $(t_\alpha/t_{0.5})_{theo}$. By fitting the experimental values with the theoretical values, the appropriate kinetic model can be determined[23,24]. The relationship between $g(\alpha)$ and t allows for the calculation of $k(T)$. Finally, the apparent activation energy can be derived from the Arrhenius equation:

$$k(T) = A \cdot \exp(-E_a/RT) \tag{4}$$

where $k(T)$, A, R and T represent the rate coefficient of reaction, the pre-exponential factor, the molar gas constant and the tested temperature, respectively.

Theoretical calculations

DFT calculations were applied on projected augmented wave (PAW)-based Vienna *ab initio* simulation package (VASP) method, which is used for the description of exchange-correlation between the electrons combined with the generalized-gradient approximation (GGA) in the parameterization of Perdew-Burke-Ernzerhof (PBE) pseudopotential to the electrons[25,26]. The selected models for Zr_2Fe (mp-1159), ZrH_2 (mp-24286), and Zr_2FeH_5 (mp-643907) from the Materials Project and Zr_2FeH_2 from the Inorganic Crystal Structure Database were subjected to geometrical optimization. The plane wave cutoff energy was set to 380 eV; the self-consistent convergence criteria of electron and ion are respectively set to be 10^{-6} eV and 0.02 eV/Å, and 5 × 5 × 6 Gamma centered Monkhorst-Pack grid k-points are employed for corresponding structure optimizations. The visualization and annotation of the models were achieved by Visualization for Electronic and Structure Analysis (VESTA)[27], and the projected density of states (PDOS) was further determined and then projected using P4VASP. The chemical bonding analysis of Metal-H interaction was carried out using the crystal orbital Hamilton population (COHP), which was calculated by the Local Orbital Basis Suite Toward Electronic-Structure Reconstruction code (LOBSTER)[28]. The integral of the COHP (ICOHP) describes the bond strength by integrating energy below Fermi energy[29].

RESULTS AND DISCUSSION

The phase composition and crystal structure of the Zr_2Fe sample were confirmed by XRD, as shown in Figure 1A, where most of the diffraction peaks match well with tetragonal Zr_2Fe (JCPDS no. 04-003-5495, space group: I4/mcm). The diffraction peaks at 35.3°, 42.9° and 44.9° respectively correspond to the (211), (202) and (310) planes of tetragonal Zr_2Fe. Besides, three obvious diffraction peaks located at 38.4°, 41.9° and 65.0° can be seen, corresponding well to the (511), (440) and (822) planes of cubic Zr_2Fe (JCPDS no. 04-002-9744, space group: Fd3m). The crystal structure phase composition was analyzed by Rietveld refinement, and the weighted ratio of tetragonal Zr_2Fe and cubic Zr_2Fe is obtained as 86.5:13.5. Figure 1B presents a SEM image with energy dispersive X-ray spectroscopy (EDX) elemental mapping of Zr_2Fe powder. The distribution regions of the Zr and Fe elements are basically consistent with the area of Zr_2Fe, demonstrating the compositional homogeneity of Zr_2Fe.

Hydrogen storage performance of Zr_2Fe is greatly correlated with the condition of activation. Evacuation at high temperatures tends to dissociate the impurity gas adsorbed on the surface of the Zr_2Fe alloy. A method of thermal vacuum degassing experiment was conducted to investigate the relationship between temperature and activation. The result [Figure 1C] clearly exhibits a direct relationship between temperature and the intensity of impurity gas desorption, demonstrating that the impurity desorption is concentrated at 200~300 °C and lasts until 430 °C, thereby guiding the activation procedure of Zr_2Fe. Figure 1D presents the XRD pattern of the sample after activation; it is found that the crystal phase

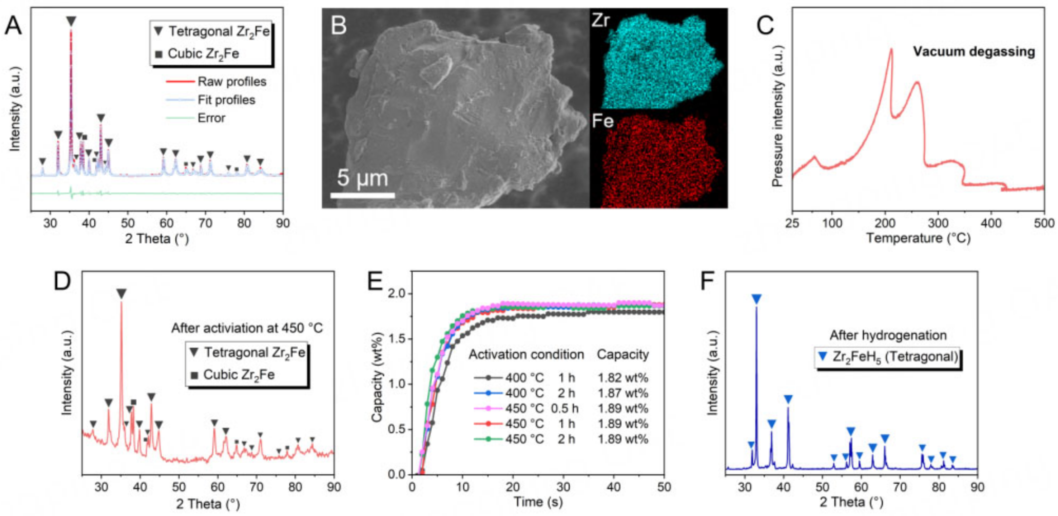

Figure 1. XRD pattern (A) and SEM image correlating the EDX mapping micrographs (B) of as-cast Zr_2Fe alloy; (C) Pressure *vs.* temperature during thermal vacuum degassing activation experiment; (D) XRD pattern of activated Zr_2Fe alloy; (E) Hydriding kinetics of Zr_2Fe after different activation conditions; (F) XRD pattern of Zr_2FeH_5 hydride. XRD: X-ray diffractometer; SEM: Scanning electron microscope; EDX: Energy dispersive X-ray spectroscopy.

composition and structure of as-cast Zr_2Fe are maintained, indicating that only trace impurities covering the surface are removed. Subsequently, the hydriding kinetics with a reactant loading of 0.25 g were tested to assess the hydrogenation performance at 1 bar and the effect of activation condition [Figure 1E]. Under activation conditions of 400 °C/2 h and 400 °C/1 h (vacuuming), the former exhibits faster kinetics, with a higher hydrogen storage capacity of 1.87 wt%, indicating that impurities desorption rate is relatively low at 400 °C. Furthermore, after vacuuming at 450 °C for 0.5 h, rapid kinetics can be achieved, with a hydrogen storage capacity reaching 1.89 wt%. There is no significant further improvement in hydrogen absorption performance at longer activation durations at 450 °C, which is consistent with the vacuum degassing experiment. The XRD pattern of the hydrogenation product of the Zr_2Fe alloy is shown in Figure 1F; it is found that both tetragonal Zr_2Fe and cubic Zr_2Fe are hydrogenated to tetragonal Zr_2FeH_5, forming a single-phase structure.

The hydrogen storage properties and thermodynamic parameters of Zr_2Fe alloys were further investigated through de-/hydrogenation PCT tests (10^{-5}~10 bar) and the Van't Hoff calculation. It can be observed that Zr_2Fe exhibits sloped de-/hydrogenation PCT curves at 325, 350 and 375 °C [Figure 2A]. It is worth mentioning that the hydrogen pressure corresponding to the midpoint of the saturation capacity (~ 1 wt%) is adopted as equilibrium hydrogen pressure (P_{eq}) due to the non-significant plateau properties of the PCT curves. It can be obtained that the hydrogenation equilibrium pressures are 305, 777 and 1,800 Pa at 325, 350 and 375 °C, respectively, and the dehydrogenation equilibrium pressures are 213, 540 and 1,295 Pa. Due to the difference of lattice strain during the de-/hydrogenation, there is little hysteresis between absorption and desorption processes[30]. For dehydrogenation at 375 ℃, the hydrogen background pressure of 200 Pa can only make the dehydrogenation capacity reach 0.99 wt%, much lower than the corresponding saturation capacity, indicating the incomplete dehydrogenation due to the excessively low equilibrium pressure of Zr_2Fe. Deeper dehydrogenation of Zr_2Fe hydride requires a higher temperature and continuous ultra-high vacuum environment.

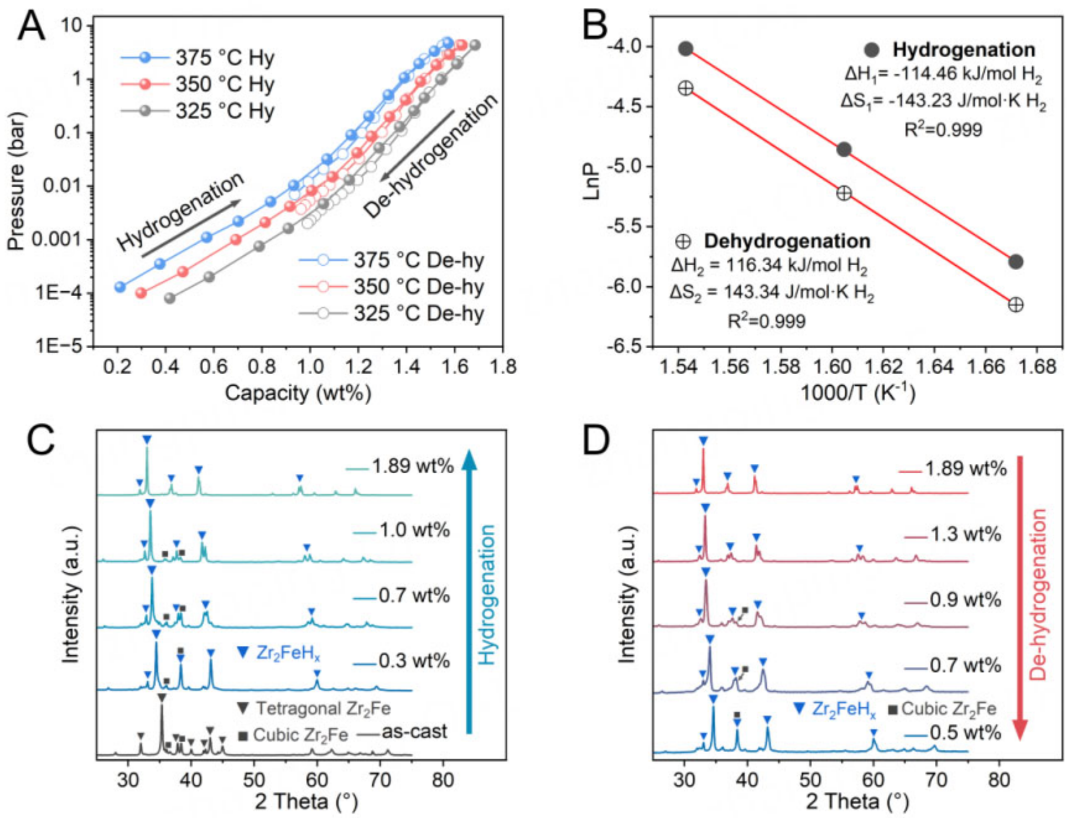

Figure 2. Hydrogenation and dehydrogenation PCT curves of Zr_2Fe samples at different temperatures (A) and their corresponding Van't Hoff plots (B); XRD patterns of hydrogenated (C) and dehydrogenated (D) Zr_2Fe corresponding to different cutoff capacities. PCT: Pressure-ccomposition-temperature; XRD: X-ray diffractometer.

The Van't Hoff calculation is shown in Figure 2B. The de-/hydrogenation thermodynamic parameters have been calculated in terms of the P_{eq} at different temperatures (T) using[31]:

$$\ln P_{eq} = - \Delta H/RT + \Delta S/R \tag{5}$$

Where ΔH and ΔS are enthalpy and entropy change of reaction, while R and T are the molar gas constant and the experimental temperature, respectively. The specific thermal parameters including ΔH and ΔS, listed in Figure 2B, are obtained from the fitting curves of Van't Hoff plots. The calculated hydrogenation enthalpy of the Zr_2Fe-H system is -114.46 kJ/mol H_2, slightly lower than that of the Zr_2Co-H system[14], laterally indicating similar hydrogenation behavior between these two systems. According to Van't Hoff equation, significantly low hydrogenation P_{eq} (25 °C) of Zr_2Fe was acquired as 2.68×10^{-8} Pa, which is several orders of magnitude lower than the equilibrium pressure of Zr_2Co (3.22×10^{-6} Pa) and ZrCo (10^{-3} Pa). This makes Zr_2Fe ideal for capturing low concentrations of hydrogen isotopes, improving the safety and effectiveness of the TEP system.

To further study the phase transition behaviors during de-/hydrogenation in Zr_2Fe-H system, the Zr_2Fe hydrides with various hydrogen concentrations in the process of hydrogen absorption and thermal desorption were intercepted for XRD analysis [Figure 2C and D]. In the initial hydrogenation (0~0.3 wt%), the tetragonal Zr_2Fe phase transforms into the Zr_2FeH_x phase. Observably, the diffraction peaks at 35.3° and 44.9° are shifted to a smaller angle of about 1°, which represents a sharp expansion in the corresponding

(211) and (310) interplanar spacing. Some diffraction peaks at 32°, 37.9° and 43° corresponding to the (002), (112) and (202) crystal planes, respectively, are significantly shifted to larger angles. The lattice calculations [Table 1] demonstrate that the lattice parameters *a* and *b* of the tetragonal structure are expanding, while *c* is shrinking. At this stage, the crystal distortion and the significant expansion of 1.75% per 0.1 wt% on average indicate the rapid atomic migration as Zr_2Fe is hydrogenated. During 0.3~1.89 wt% hydrogen absorption, the diffraction peaks of Zr_2FeH_x are continuously shifted to smaller angles, and the lattice shows an expansion trend. In contrast, the cubic Zr_2Fe exhibits slower kinetics and higher hydrogenation energy barriers, and is gradually hydrogenated during the later stage of absorption to co-form the tetragonal Zr_2FeH_5. Overall, it appears that the lattice of Zr_2Fe exhibits anisotropic expansion during hydrogenation, with sharp distortions and expansions in the lattice at the early stage of hydrogen absorption, followed by progressively smaller expansions at the later stage. This is consistent with our computational optimization results [Supplementary Table 1]. During dehydrogenation, the diffraction peaks of Zr_2FeH_x are continuously shifted to higher angles, in which the H atoms are progressively removed from the Zr_2FeH_x, resulting in lattice contraction. Along with this, the cubic Zr_2Fe alloy is preferentially obtained, suggesting that it has a relatively high hydrogen equilibrium pressure. The XRD pattern of the further dehydrogenated product [Supplementary Figure 1] exhibits the phase transition from hydride to alloy phase. The diffraction peak corresponding to the Zr_2FeH_x (211) plane progressively shifts to the large angle until it correlates to the (211) plane of Zr_2Fe. In addition, the diffraction peaks corresponding to the (202) and (310) planes of the hydride are separated after both shifting to about 43°, and then the peak corresponding to the (310) plane continually shifts to 44.7°, which corresponds to the Zr_2Fe phase, indicating the further variation in the lattice structure due to the dissociation of H atoms in certain interstices. Simultaneously, the peaks formed at 31.9° and 39.7° also correspond to the Zr_2Fe phase. This process can be regarded as a reverse transition of hydrogenation. Thus, the de-/hydrogenation reactions of the sample can be expressed as:

$$Zr_2Fe\ (\text{tetragonal/cubic}) + H_2 \rightleftarrows Zr_2FeH_5\ (\text{tetragonal}) \quad (6)$$

For Zr-based HSAs, the occurrence of disproportionation reactions is inevitable for removing more hydrogen at higher temperatures. Thus, the factors influencing disproportionation of Zr_2Fe need to be critically considered. Initially, rapid hydrogenation experiments were conducted, as shown in Figure 3A. Given that the hydrogenation of Zr_2Fe is an exothermic reaction as mentioned above, the exothermic heat can result in instantaneous temperature rise during the hydrogen absorption of Zr_2Fe to saturation, and the higher quantity of the reactant loading in a fixed-volume reactor can generate more exothermic heat in a comparable time. The corresponding XRD analyses of the products [Figure 3B] need to be discussed in conjunction. It can be found that the sample with loading 0.25 g exhibits a maximum surge temperature of 78 °C and achieves the rated hydrogen storage capacity of Zr_2Fe alloys (1.89 wt%) during hydrogenation. The XRD results indicate that the product is predominantly composed of Zr_2FeH_5, suggesting that the relatively low-temperature fluctuation (78 °C) is insufficient to induce a disproportionation reaction. At the sample loading of 1.5 g, the maximum surge temperature reaches 416 °C and the hydrogen storage capacity drops to only 1.67 wt%. At this point, it is clear that Zr_2FeH_5 is considered the principal phase, where some impurity phases such as ZrH_2 and $ZrFe_2$ located at 32.3° and 42.3°, respectively, are identified as disproportionation phases. Evidently, as the sample loading further increases to 2 g, the disproportionation becomes more severe. The intensification of temperature rise during reaction greatly damages hydrogen storage performance, and there is a strong correlation between them [Supplementary Figure 2]. It can be inferred that the increased thermal motion of the atoms at elevated temperatures leads to more unstable positions in the crystals, which may promote the generation of disproportionation phases.

Table 1. The lattice parameters of Zr_2Fe at different stages of hydrogenation

Hydrogenation stages	Lattice parameters (Å)			Volume (Å^3)	Average expansion rate per 0.1 wt%
	a	b	c		
Zr_2Fe	6.369	6.369	5.591	226.771	1.75% (0~0.3 wt%)
0.3 wt%	6.643	6.643	5.408	238.670	1.31% (0.3~0.7 wt%)
0.7 wt%	6.794	6.794	5.442	251.205	0.77% (0.7~1.0 wt%)
1.0 wt%	6.846	6.846	5.484	257.034	0.58% (1.0~1.89 wt%)
1.89 wt%	6.932	6.932	5.624	270.268	

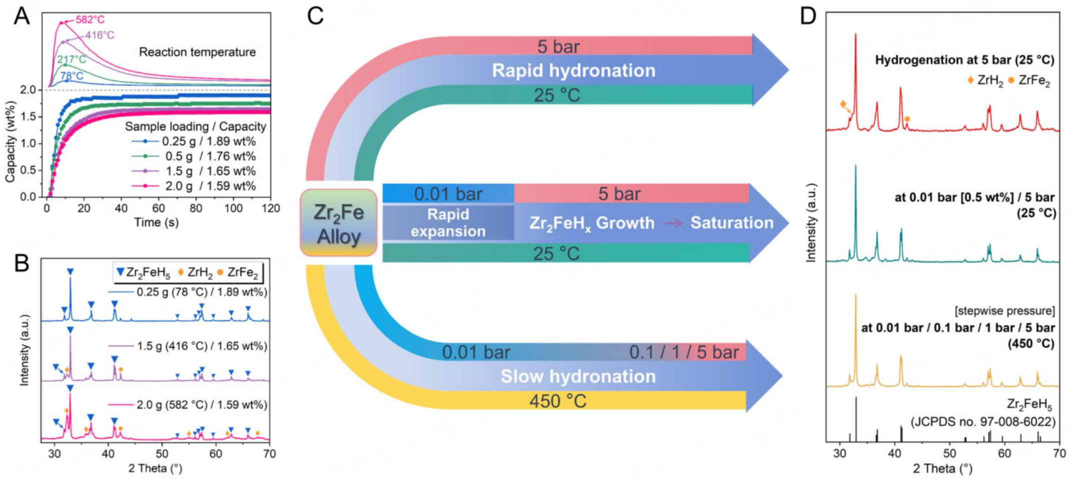

Figure 3. Hydriding kinetics (initial pressure: 1 bar) of Zr_2Fe with different sample loadings (A) and XRD patterns of the corresponding products (B); The schematic diagram of hydrogenation process with different pressures and temperatures (C) and XRD patterns of hydrogenation products of Zr_2Fe under corresponding hydrogenation conditions (D). XRD: X-ray diffractometer.

In order to further investigate the triggering mechanism of disproportionation, a series of rapid hydrogenation experiments with different configurations of pressure and temperature are conducted, as depicted in Figure 3C, and the corresponding XRD analyses of products are shown in Figure 3D. It reveals that certain disproportionation products will be produced during the process of over-rapid hydrogenation to saturation of Zr_2Fe (The maximum surge temperature is 37 °C). This result suggests that excessively rapid insertion of H atoms can induce disproportionation, and the thermodynamic condition of disproportionation is easy to satisfy. Meanwhile, PCT tests for hydriding disproportionation were conducted, and the ΔH and ΔS of the reaction were obtained, with values of -174.79 kJ/mol H_2 and -141.12 J/K·mol H_2, respectively [Supplementary Figure 3]. The value of ΔH is much lower than that of the general hydrogenation (-114.46 kJ/mol H_2), further confirming the thermodynamic explanation of the disproportionation reaction discussed above. In the other way, Zr_2Fe was first hydrogenated to 0.5 wt% capacity at 0.01 bar, and then rapidly hydrogenated at 5 bar. No disproportionation phases are observed in the saturated hydride, indicating that the crystal structure is more stable in the latter part of the hydrogenation. This well corresponds with the above XRD lattice structure analysis of the hydrogenation stage, further supported by the fact that disproportionation is tendentiously induced by the dramatic crystal expansion or the rapid migration of atoms. As mentioned above, high temperature is one of the triggers for disproportionation. However, no disproportionation phase is observed in the mildly hydrogenated product at a constant 450 °C (higher than the peak temperature in the above rapid hydrogenation experiments with obvious disproportionation: 416 °C). The contrast further demonstrates that the occurrence of disproportionation requires not only the satisfaction of thermodynamic conditions but also kinetic conditions, and the rapid atomic migration facilitates overcoming the disproportionation energy barrier.

Further investigation found that disproportionation can be induced by high temperatures at low pressures as well, because the high temperature may enhance the atomic thermal motion to deliver additional energy for disproportionation to overcome the kinetic barrier. Unfortunately, the high-temperature environment is the primary cause of disproportionation in actual applications, and thus should be given particular consideration. However, at high temperatures, the measured values of hydrogen storage equilibrium pressures and capacities are implicated by the interference of hydriding disproportionation behavior, making it impossible to accurately measure the general hydrogenation PCT curves at high temperatures. According to the special hydrogenation phase transition behaviors of Zr_2Fe, we calculated the high-temperature general hydrogenation PCT curves by inversion of the Van't Hoff equation based on the discrete points of 325~375 °C PCT curves, as shown in Figure 4A, where the curves at 450 °C and 500 °C well match the experimentally measured curves. This provides a reference for subsequent temperature-dependent hydrogenation and hydriding disproportionation studies. Then, low-pressure hydrogen absorption experiments at various elevated temperatures were performed to explore the fundamental relationship between temperature and disproportionation behavior [Figure 4B]. From the above, it is known that the hydrogenation reaction ($Zr_2Fe \rightarrow Zr_2FeH_x$) occurs preferentially during slow hydrogen absorption at high temperatures; thus, we hydrogenated the samples and controlled the hydrogenation equilibrium to 1,000 Pa at each tested temperature, so that the subsequent hydriding disproportionation was performed in a normalized manner. Figure 4C shows the XRD patterns of the corresponding products. Observations indicate that the hydrogen pressure remains almost stable in the latter stage at 350 °C, while the hydrogen absorption due to disproportionation is essentially invisible throughout the whole procedure. At 375 °C, hydrogen absorption noticeably accelerates, and the faint ZrH_2 diffraction peak can be observed in the XRD pattern of the product. Additionally, there is no indication of pressure balancing at 75,000 s, suggesting that the disproportionation reaction is still continuously proceeding. The phenomenon of gradual disproportionation reaction becomes more pronounced at 400 °C, and ZrH_2 becomes clearly discerned at the end of the procedure. Subsequently, the rate of disproportionation reaction increases dramatically with temperature, causing the hydrogen pressure to reach final equilibrium more rapidly at 450 °C and 500 °C, while the samples are eventually almost disproportionated. In the absence of rapid atomic migration and with the satisfaction of disproportionation thermodynamics, the disproportionation reaction is continuously triggered with increasing temperature. This phenomenon can be interpreted as the fact that the hydriding disproportionation reaction requires a higher temperature to overcome the kinetic energy barrier. Consequently, temperature is the primary factor that supports the kinetic behaviors of the hydriding disproportionation reaction in the Zr_2Fe-H system in practice.

To confirm the aforementioned conjecture, the apparent activation energy (E_a) was introduced to provide a more detailed explanation. A practical approach for finding kinetic models was adopted for the hydriding disproportionation reaction, as illustrated in Figure 5A-D. Figure 5A exhibits the relative kinetics performance for the hydriding disproportionation reaction across the temperature range of 550 to 625 °C, where the reaction kinetics gradually slow down with the increasing extent of reaction. In contrast, Figure 5B shows the plots based on the experimental value $(t/t_{0.5})_{exp}$ *vs.* the modeled theoretical value $(t/t_{0.5})_{theo}$, where t represents the time corresponding to the reaction progress fraction α, and $t_{0.5}$ stands for the time when $\alpha = 0.5$. The experimental data were fitted with nine different models [Figure 5B], and the linear slopes of the fitted lines were summarized. Previous studies have confirmed that the slope of the fitted line [Figure 5B] should be close to 1 for a matched kinetic model. Remarkably, the three-dimensional phase boundary model (R3) exhibits the best linear relationship with a slope value of 1.0434 and a correlation coefficient (R^2) of 0.999, suggesting that the hydriding disproportionation reaction is closely associated with

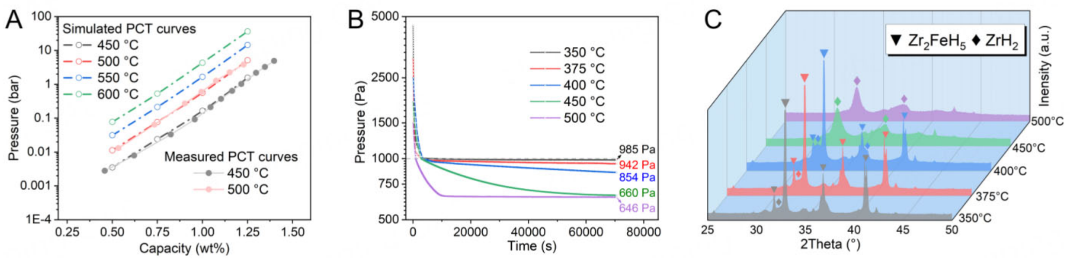

Figure 4. (A) Simulated/measured hydrogenation PCT curves of Zr_2Fe-H system at 450~600 °C; Controlled hydrogen absorption curves of Zr_2Fe at 350~500 °C (B) and XRD of the corresponding hydrogenation products (C). PCT: Pressure-ccomposition-temperature; XRD: X-ray diffractometer.

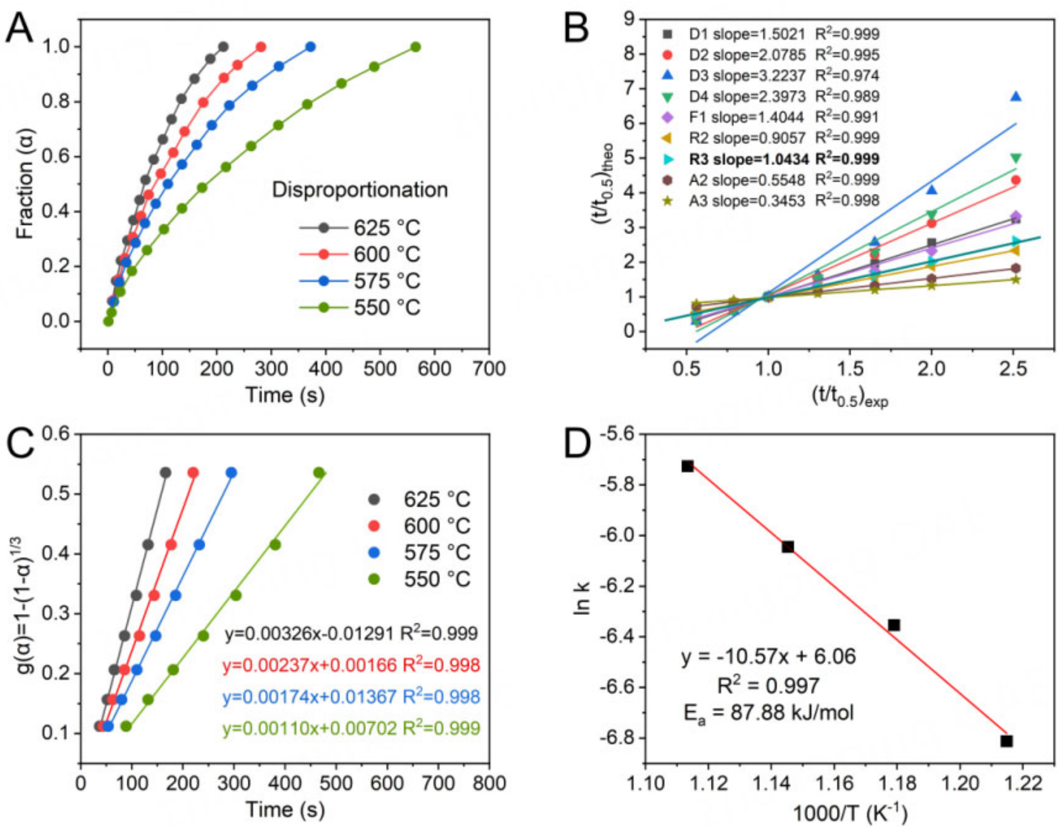

Figure 5. (A) The normalized kinetics curves of hydriding disproportionation reaction; (B) Comparison of different kinetic models; (C) Fitting results of kinetics curves with R3 model; (D) Activation energy calculation using Arrhenius plot.

phase-boundary controlled reaction (contracting volume, i.e., tridimensional shape). The hydriding disproportionation solid-state kinetics model of Zr_2Fe is consistent with that of ZrCo obtained through different testing methods, both following the R3 model[32]. This corroborates a similar behavior pattern between Zr atoms and H in the Zr-based alloy. The plots of the proposed kinetic mechanism [R3: $g(\alpha)$ $1-(1-\alpha)^{1/3}$] *vs.* time for the hydriding disproportionation reaction are displayed in Figure 5C, where all curves exhibit good linearity, demonstrating that in fact the reaction kinetics can be reasonably explained by the R3 model. The R3 model describes that the disproportionation processes in our case have close relationships with diffusion. Its reaction mechanism belongs to geometrical contraction models, which assume that the disproportionation reaction occurs rapidly on the surface of Zr_2Fe and that the rate is controlled by the resulting reaction interface progress toward the center[23,33-35]. Meanwhile, the ZrH_2 shell around the unreacted Zr_2Fe nuclei is formed, which will impede the latter penetration of H atoms into the fresh nucleation sites and interfaces inside particles. This kinetic behavior is supposed to be more pronounced at relatively low hydrogen densities and temperatures. In addition, the R3 model is believed to be related to the contracting volume of particles; thus, a sample of varying particle sizes may have a variable disproportionation reaction rate. According to the rate constants $k(T)$ of the disproportionation reaction at different temperatures derived from Figure 5C, the E_a can be calculated using the Arrhenius equation (4). The results are presented in Figure 5D. There is a good fit of ln $k(T)$ *vs.* 1000/T with R^2 = 0.997, and E_a was calculated as 87.88 kJ/mol, which is lower than that of the ZrCo alloy (147.8 kJ/mol)[32]. This implies that the disproportionation reaction for Zr_2Fe is more easily triggered, and the relatively low activation energy may be attributed to the higher abundance of Zr sites in the Zr-rich alloys.

Furthermore, the reaction pathways of the hydriding disproportionation should be investigated clearly. Firstly, we selected the temperature of 500 °C at which disproportionation is pronounced in the thermostatic hydrogenation test [Figure 6A]. As presented in Figure 4A, it is evident that the equilibrium pressure remains low in instances of low hydrogen capacity fractions. Thus, it can be noticed that even at the low hydrogen pressure of 0.03 bar and 500 °C, the initial process still exhibits a relatively rapid kinetics hydrogen absorption. The XRD pattern of the intermediate state [Figure 6B] indicates that Zr_2Fe has been fully hydrogenated to Zr_2FeH_x ($1 < x < 2$) at Point A. Subsequently, the hydrogen-absorbing reaction with slower kinetics can be remarkably distinguished, as its final product is predominantly the disproportionation phase according to the XRD pattern of Point B [Figure 6B]. This identifies Point A as the transition point between general hydrogenation and disproportionation, and the Zr_2Fe will be preferentially hydrogenated above the equilibrium pressure of hydrogenation. Consequently, one of the disproportionation paths is confirmed as:

$$Zr_2FeH_x + H_2 \rightarrow ZrH_2 + ZrFe_2 \tag{7}$$

The procedure of Point A to C corresponds to thermal preservation for 10 h with isolation of almost all hydrogen. The XRD pattern of the product suggests that only a part of Zr_2FeH_x transforms to ZrH_2 and $ZrFe_2$, consuming the residual hydrogen inside the container. While the diffraction peaks of hydride are still obvious, with a right shift of 0.4° in comparison to Point A, as Zr_2FeH_x ($0 < x < 1$), suggesting that partial H atoms have been detached from hydride due to the decrease in hydrogen pressure. This result demonstrates that, during the transition from Point A to C, the following reaction occurs in addition to reaction (7).

$$Zr_2FeH_x \rightarrow Zr_2Fe + H_2 \tag{8}$$

Furthermore, both reactions (7) and (8) are also expected to occur in a sufficient hydrogen environment such as Point A to B; however, in such a scenario, reaction (8) will be significantly diminished and reaction (7) becomes the competitively dominant reaction.

Whether Zr_2Fe can be directly disproportionated was further discussed. The tested temperature was increased to 600 °C to elevate the hydrogenation equilibrium pressure. Simultaneously, a lower hydrogen pressure (0.01 bar) was given to allow only trace amounts of hydrogen to be initially dissociated [Figure 6C]. The XRD pattern in Figure 6D displays the presence of the principal Zr_2Fe phase and less amount of ZrH_2 phase in the intermediate state (5 min). Notably, disproportionation reaction can still occur, which definitively suggests that Zr_2Fe can undergo direct disproportionation as follows:

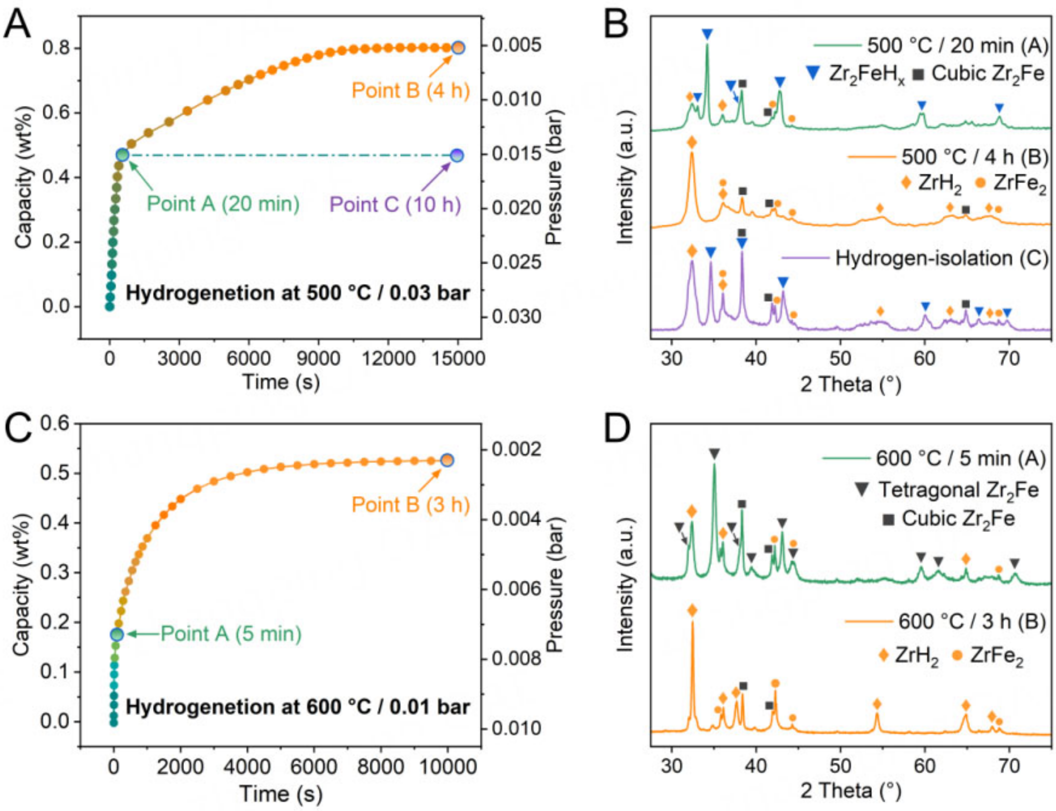

Figure 6. Kinetic tests for Zr_2Fe samples under 500 °C/0.03 bar and 600 °C/0.01 bar H_2 (A, C) and the corresponding XRD patterns for the marked point (B, D). XRD: X-ray diffractometer.

$$Zr_2Fe + H_2 \rightarrow ZrH_2 + ZrFe_2 \tag{9}$$

In the end, due to the low pressure of 200 Pa, the disproportionation reaction lacks the necessary driving force to fully form into the ZrH_2 and $ZrFe_2$ phases, leaving residual small amounts of cubic Zr_2Fe. The crystallization of the disproportionation products was promoted at higher temperatures, indicating a stronger interaction between Zr and H[36,37].

The aforementioned study on dehydrogenation phase transition has indicated that disproportionation phases will be generated during the high-temperature dehydrogenation of Zr_2Fe hydrides. Therefore, we performed TPD experiments under hydrogen pressures kept within 1,000 Pa to investigate the dehydrogenation behaviors over a wide temperature range, as depicted in Figure 7A and B. It can be seen that the dehydrogenation evenly occurs below 500 °C, with a small dehydrogenation peak observed at about 200 °C. The slope of the curve begins to decline obviously around 500 °C and then continues to decrease until 600 °C, reflecting the occurrence of hydrogen absorption and the gradual obscuration of dehydrogenation. Later, the slope gradually rises, followed by a vigorous hydrogen release after 670 °C, attributed to the decomposition of ZrH_2[14]. This process corresponds to the exothermic and endothermic reactions observed in the DSC curve of the Zr_2FeH_5 [Supplementary Figure 4]. One thing to mention: according to reaction (7), the hydriding disproportionation reaction occurs when the x of Zr_2FeH_x is less than 3, and the disproportionation reaction from Zr_2FeH_x ($3 < x < 5$) is regarded as dehydriding disproportionation reaction. When Zr_2FeH_5 is subjected to certain high pressures and temperatures, dehydriding disproportionation occurs instead of general dehydrogenation [Supplementary Figure 5],

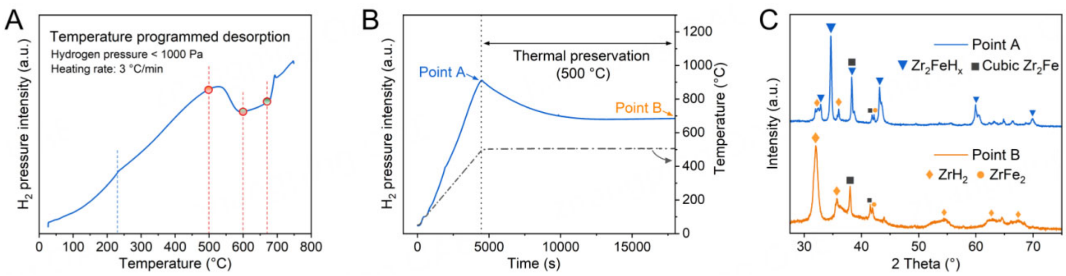

Figure 7. TPD curves of Zr_2FeH_5 at the temperature range of 25~750 °C (A) and 25~500 °C (B); and XRD patterns for the marked points (C). TPD: Temperature-programmed dehydrogenation; XRD: X-ray diffractometer.

apparently indicating that the equilibrium pressure of dehydriding disproportionation is much higher than that of general dehydrogenation. Thus, the dehydriding disproportionation reaction is definitely accompanied by a dehydrogenation process of Zr_2FeH_x ($3 < x < 5$) at high temperatures above 375 °C. Furthermore, the above-mentioned investigation found that the dehydrogenated product of Zr_2FeH_x with x less than 3 can be obtained when dehydrogenation is below the critical temperature of disproportionation (375 °C). Therefore, in our experiments and practical applications, the dehydriding disproportionation reaction can almost be avoided.

Subsequently, we set 500 °C as the peak temperature, where the slope observably decreases in Figure 7A, and implemented a heating-preservation dehydrogenation program, as depicted in Figure 7B. Here, the XRD characterization of turning Point A and Point B was carried out respectively, as displayed in Figure 7C. During the heating dehydrogenation, Zr_2FeH_x was dehydrogenated to the x value of about 1.2 as heating to 500 °C (Point A), with almost no disproportionation occurring. It is evident that the sample switches to lower hydrogen release after temperature stabilization, while the hydriding disproportionation reaction (7) continues until Point B. The explanation can also be derived that the side reaction of hydriding disproportionation intensifies with increasing temperature at a range of 375 to 600 °C when the sample interacts with H progressively. Furthermore, the gradual decrease of the curve slope in Figure 7A demonstrates that dehydrogenation and hydriding disproportionation can occur simultaneously. This brings out the importance of inhibiting the disproportionation reaction.

Figure 8A displays the optimized lattice structures of Zr_2Fe, Zr_2FeH_2, Zr_2FeH_5, $ZrFe_2$ and ZrH_2, and the corresponding schematic illustration for de-/hydrogenation and disproportionation. The de-/hydrogenation can be modulated depending on the temperature and hydrogen pressure, while above 375 °C, the disproportionation reaction will aggressively compete for the reactants Zr_2Fe/Zr_2FeH_x. Kinetic activation energy and thermodynamic principles have been utilized to explain the apparent mechanism of de-/hydrogenation and disproportionation. Furthermore, DFT calculations were introduced to further investigate intrinsic causes of the behaviors of Zr_2Fe alloy interacting with hydrogen. Herein, the hydrogen removal energy $E_r(H)$ is defined as follows:

$$E_r(\mathrm{H}) = E_1 + E_\mathrm{H} - E_0 \tag{10}$$

where $E_r(H)$ represents the required energy for removing one particular H atom within the lattice, and E_H is the energy of single H atom. E_1 and E_0 denote the energy of optimized structure with and without removal of single H atom, respectively.

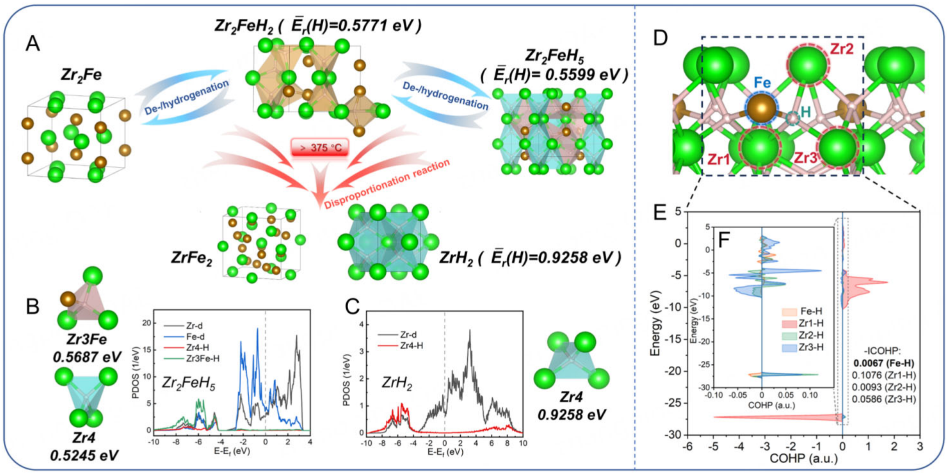

Figure 8. (A) The schematic illustration of the relationship between hydrogenation, dehydrogenation and hydrogen-induced disproportionation in Zr_2Fe-H system with lattice structures of Zr_2Fe, Zr_2FeH_2, Zr_2FeH_5, $ZrFe_2$ and ZrH_2; PDOS and interstices diagram of Zr_2FeH_5 (B) and ZrH_2 (C); A typical example of Zr3Fe interstices (D) and calculated COHP between Zr, Fe and H in Zr3Fe (E and F). PDOS: Projected density of states; COHP: Crystal orbital hamilton population.

According to the chemical environment of H atoms in the specific tetrahedral interstitial sites, different types of hydrogen interstice were segmented and rendered for clearer visualization. The interstices of Zr_2FeH_5 can be divided into two types: Zr3Fe and Zr4, with a quantity ratio of 4:1 in one unit cell. The PDOS [Figure 8B] shows a clear hybridization of d-orbital between Zr and Fe atoms in Zr_2FeH_5, and a significant weakening of interactions between Zr and H atoms in the Zr4 interstitial sites within the energy range of -6.5 to 5 eV[38]. Furthermore, the average E_r(H) of the Zr4 (0.5245 eV) is correspondingly lower than that of Zr3Fe (0.5687 eV). In contrast, the H atoms are only located in the Zr4 interstices in the ZrH_2 unit cell, and the PDOS [Figure 8C] also presents a strong interaction of H and d-orbital of Zr atoms, which result in a remarkably higher average E_r(H) for this Zr4 site (0.9258 eV).

Based on this foundation, the weighted average E_r(H) of the above three hydrides was calculated, respectively. For Zr_2FeH_2, there is one type of tetrahedral interstice, Zr3Fe. Therefore, it can be inferred that hydrogen preferentially occupies the Zr3Fe interstice with relatively high hydrogen binding energy in the early stage of hydrogenation. As the hydrogenation proceeds, the Zr4 interstices with relatively low hydrogen binding energy are filled posteriorly. This coherently corresponds to the lattice variation during the Zr_2Fe hydrogenation, where larger energy variations respond to larger H-induced lattice distortions, implying that the hydrogen insertion and atomic migration overcome more resistance in the prior hydrogenation[39-42]. Furthermore, with the average E_r(H) of Zr_2FeH_5 (0.5599 eV) being lower than that of Zr_2FeH_2 (0.5771 eV), it implies that Zr_2FeH_5 tends to decompose into Zr_2FeH_2 with relatively good stability of hydride. Simultaneously, the distance between the hydrogen atoms during dehydrogenation progressively increases, which leads to a lower collision probability of dissociative H atoms; therefore, the energy required for dehydrogenation increases as the process proceeds. The cleavage of Zr-H and Fe-H bonds and the formation of H-H bonds are correlative causes affecting dehydrogenation[43].

During hydriding disproportionation at high temperatures, the energy barrier of disproportionation reaction is activated, and Zr_2FeH_x is progressively converted to ZrH_2 and $ZrFe_2$, which implies that the disproportionation process induced by high temperatures is accompanied by the breaking of Metal-H bonds in the Zr_2FeH_x structure. Thus, we measure the metal and hydrogen interactions and qualify the bonding strength in Zr3Fe [Figure 8D] based on the COHP method, as shown in Figure 8E and F.

The ICOHP values at the Fermi level signify the energy contribution of bonding electrons shared between two atoms, and accurately reflect the strength of the bond. By definition, a more negative value of ICOHP suggests stronger bonding[29]. The absolute values of ICOHP crossing the Fermi level for Zr1-H, Zr2-H, Zr3-H and Fe-H bonds in Zr3Fe interstice were calculated as 0.10760, 0.0093, 0.0586 and 0.0067 eV, respectively. It follows that there is a positive correlation between the dehydrogenation energy barrier in the Zr_2Fe-H system and the strength of the stronger Zr1-H and Zr3-H bonds in the Zr3Fe interstices. Significantly, the ICOHP absolute value of Fe-H is calculated to be less than that for Zr-H bonds, suggesting that the Fe-H bond in the Zr3Fe-H is supposed to break more easily due to weak covalent interactions between Fe and H atoms. At temperatures that induce disproportionation, the Zr atoms tend to combine with H to form the disproportionation product of ZrH_2, due to the significantly higher average E_r(H) of ZrH_2 (0.9258 eV) compared with Zr_2FeH_2 (0.5771 eV) and Zr_2FeH_5 (0.5599 eV). Meanwhile, the Fe-H bond may preferentially break, causing an inhomogeneous chemical environment due to the incoordination of Zr and Fe atoms, and creating a driving force for segregation into the Fe-rich phase of $ZrFe_2$, promoting disproportionation reaction. As a result, Zr_2Fe/Zr_2FeH_x in any state tends to be transformed into the compound $ZrFe_2$ and ZrH_2 with stronger hydrogen removal energy once the triggering conditions for disproportionation are met. The lattice destabilization caused by high temperature, large lattice structure changes and the rapid migration of atoms can help induce the disproportionation reaction. These collectively explain the competitive predation of disproportionation reaction over the general de-/hydrogenation.

CONCLUSIONS

In summary, the de-/hydrogenation behaviors of the Zr_2Fe-H system and their corresponding kinetic and thermodynamic characteristics have been comprehensively investigated. The ultra-low hydrogenation equilibrium pressure of Zr_2Fe at 25 °C is determined as 2.68×10^{-8} Pa, and the thermodynamic parameters of enthalpy change ΔH and entropy change ΔS are -114.46 kJ/mol H_2 and -143.23 J/K·mol H_2 in hydrogenation reaction, while the ΔH and ΔS of the dehydrogenation are calculated as 116.34 kJ/mol H_2 and 143.34 J/K·mol H_2, respectively. Herein, key reference data of the relationship between the equilibrium pressure and various high temperatures (450~600 °C) were obtained according to the thermodynamic relationships. These data are utilized to profile the hydrogenation properties of Zr_2Fe at high temperatures and distinguish between hydrogenation and hydriding disproportionation. The analysis suggests that the thermodynamic conditions for the hydriding disproportionation reaction are readily met; however, the reaction is subject to kinetic constraints. Further studies are needed to identify the triggering conditions and pathways (reactions 7&9) for disproportionation, and examine the interactions between disproportionation and de-/hydrogenation under various conditions. Sufficient energy, lattice variation, and atomic migration can contribute to overcoming the energy barrier for the disproportionation reaction (87.88 kJ/mol), inducing the hydriding disproportionation. Meanwhile, DFT calculations on crystal structure, hydrogen removal energy, and Metal-H bonding strength further demonstrate the unique phase transition mechanism of de-/hydrogenation and disproportionation behaviors. These results provide guidance for the performance optimization of the Zr_2Fe-H system in practical applications.

DECLARATIONS

Authors' contributions

Conceived the idea and designed the experiments: Yang, Z.; Chen, L.

Completed theoretical calculations and performed data interpretation: Jia, Y.; Yang, Z.

Supported equipment option and experimental data analysis: Yang, Z.; Liu, Y.

Provided administrative, technical, and material support: Feng, X.; Shi, Y.; Chen, C.; Luo, W.; Ying, T.; Xiao, X.; Chen, L.

Drafted the manuscript with revisions: Yang, Z.; Xiao, X.; Feng, X.; Chen, L.

Availability of data and materials

Some results supporting the study are presented in the Supplementary Materials. Other raw data that support the findings of this study are available from the corresponding author upon reasonable request.

Financial support and sponsorship

This work was supported by the National Key Research and Development Program of China (2022YFE03170002), the National Natural Science Foundation of China (52071286 and U2030208), and the Scientific Research Fund of Zhejiang University (XY2024014).

Conflicts of interest

All authors declared that there are no conflicts of interest.

Ethical approval and consent to participate

Not applicable.

Consent for publication

Not applicable.

REFERENCES

1. Komm, M. ITER: The giant fusion reactor. Bringing a sun to earth. *Fusion. Sci. Technol.* **2020**, *76*, 696-7. DOI
2. Liang, Z.; Xiao, X.; Qi, J.; Kou, H.; Chen, L. ZrCo-based hydrogen isotopes storage alloys: A review. *J. Alloys. Compd.* **2023**, *932*, 167552. DOI
3. Anand, N.; Pati, S.; Jat, R. A.; Parida, S.; Mukerjee, S. Hydrogen isotope effect on thermodynamic properties of $Pd_{0.9}X_{0.1}$ (X = Cu, Ag and Au) alloys. *Int. J. Hydrog. Energy.* **2017**, *42*, 3136-41. DOI
4. Shuai, M.; Su, Y.; Wang, Z.; Zhao, P.; Zou, J.; Wu, S. Hydrogen absorption-desorption properties of $UZr_{0.29}$ alloy. *J. Nucl. Mater.* **2002**, *301*, 203-9. DOI
5. Yao, Z.; Xiao, X.; Liang, Z.; et al. An in-depth study on the thermodynamics and kinetics of disproportionation behavior in ZrCo-H systems. *J. Mater. Chem. A.* **2020**, *8*, 9322-30. DOI
6. Wang, F.; Li, R.; Ding, C.; et al. Recent progress on the hydrogen storage properties of ZrCo-based alloys applied in international thermonuclear experimental reactor (ITER). *Prog. Nat. Sci. Mater. Int.* **2017**, *27*, 58-65. DOI
7. Kou, H.; Huang, Z.; Luo, W.; et al. Experimental study on full-scale ZrCo and depleted uranium beds applied for fast recovery and delivery of hydrogen isotopes. *Appl. Energy.* **2015**, *145*, 27-35. DOI
8. Glugla, M.; Lässer, R.; Dörr, L.; Murdoch, D.; Haange, R.; Yoshida, H. The inner deuterium/tritium fuel cycle of ITER. *Fusion. Eng. Des.* **2003**, *69*, 39-43. DOI
9. Bhattacharyya, R.; Mohan, S. Solid state storage of hydrogen and its isotopes: an engineering overview. *Renew. Sust. Energy. Rev.* **2015**, *41*, 872-83. DOI
10. Liu, Y.; Yang, Z.; Xiao, X.; et al. Enhancing disproportionation resistance of Zr_2Co-based alloys by regulating the binding energy of H atom. *Renew. Energy.* **2024**, *233*, 121153. DOI
11. Qi, J.; Huang, X.; Xiao, X.; et al. Isotope engineering achieved by local coordination design in Ti-Pd co-doped ZrCo-based alloys. *Nat. Commun.* **2024**, *15*, 2883. DOI PubMed PMC
12. Hara, M.; Hayakawa, R.; Kaneko, Y.; Watanabe, K. Hydrogen-induced disproportionation of Zr_2M (M=Fe, Co, Ni) and reproportionation. *J. Alloy. Compd.* **2003**, *352*, 218-25. DOI
13. Ruz, P.; Sudarsan, V. An investigation of hydriding performance of Zr_{2}-$_{x}Ti_{x}Ni$ (x=0.0, 0.3, 0.7, 1.0) alloys. *J. Alloy. Compd.* **2015**, *627*, 123-31. DOI
14. Liu, Y.; Zhou, P.; Xiao, X.; et al. Deep insight of unique phase transition behaviors and mechanism in Zr_2Co-H isotope system with ultra-low equilibrium pressure. *Rare. Met.* **2024**, *43*, 212-24. DOI
15. Liu, Y.; Yang, Z.; Zhou, P.; et al. A review of classical hydrogen isotopes storage materials. *Mater. Rep:. Energy.* **2024**, *4*, 100250. DOI
16. Fukada, S.; Nishikawa, M. Empirical expression for the pressure-composition-temperature curve of the Zr_2Fe-deuterium system. *J.*

Alloy. Compd. **1996**, *234*, L7-L10. DOI

17. Prigent, J.; Latroche, M.; Leoni, E.; Rohr, V. Hydrogen trapping properties of Zr-based intermetallic compounds in the presence of CO contaminant gas. *J. Alloy. Compd.* **2011**, *509*, S801-3. DOI
18. Song, J.; Wang, J.; Hu, X.; Meng, D.; Wang, S. Activation and disproportionation of Zr_2Fe alloy as hydrogen storage material. *Molecules* **2019**, *24*, 1542. DOI PubMed PMC
19. Janot, R.; Latroche, M.; Percheron-guégan, A. Development of a hydrogen absorbing layer in the outer shell of high pressure hydrogen tanks. *Mater. Sci. Eng:. B.* **2005**, *123*, 187-93. DOI
20. Pitt, M.; Pitt, L.; Fjellvåg, H.; Hauback, B. An in situ neutron diffraction study of the thermal disproportionation of the Zr_2FeD_5 system. *J. Alloy. Compd.* **2011**, *509*, 5515-24. DOI
21. Sharp, J. H.; Brindley, G. W.; Achar, B. N. N. Numerical data for some commonly used solid state reaction equations. *J. Am. Ceram. Soc.* **1966**, *49*, 379-82. DOI
22. Jones, L.; Dollimore, D.; Nicklin, T. Comparison of experimental kinetic decomposition data with master data using a linear plot method. *Thermochimica. Acta.* **1975**, *13*, 240-5. DOI
23. Xu, F.; Wang, B.; Yang, D.; Hao, J.; Qiao, Y.; Tian, Y. Thermal degradation of typical plastics under high heating rate conditions by TG-FTIR: pyrolysis behaviors and kinetic analysis. *Energy. Convers. Manage.* **2018**, *171*, 1106-15. DOI
24. Jia, Y.; Han, B.; Wang, J.; et al. Inducing one-step dehydrogenation of magnesium borohydride via confinement in robust dodecahedral nitrogen-doped porous carbon scaffold. *Adv. Mater.* **2024**, *36*, e2406152. DOI
25. Kresse, G.; Furthmüller, J. Efficient iterative schemes for ab initio total-energy calculations using a plane-wave basis set. *Phys. Rev. B.* **1996**, *54*, 11169-86. DOI
26. Forozani, G.; Mohammad, A. A. A.; Baizaee, S. M.; Gharaati, A. Structural, electronic and magnetic properties of CoZrIrSi quaternary heusler alloy: first-principles study. *J. Alloy. Compd.* **2020**, *815*, 152449. DOI
27. Momma, K.; Izumi, F. *VESTA 3* for three-dimensional visualization of crystal, volumetric and morphology data. *J. Appl. Crystallogr.* **2011**, *44*, 1272-6. DOI
28. Song, C.; Ding, F.; Ye, R.; et al. Hydrogen diffusion and anti-disproportionation properties in ZrCo alloys: the effect of Sc, V, and Ni dopants. *Int. J. Hydrog. Energy.* **2023**, *48*, 23607-19. DOI
29. Guo, X.; Zhang, S.; Kou, L.; et al. Data-driven pursuit of electrochemically stable 2D materials with basal plane activity toward oxygen electrocatalysis. *Energy. Environ. Sci.* **2023**, *16*, 5003-18. DOI
30. Qi, J.; Liang, Z.; Xiao, X.; et al. Effect of isostructural phase transition on cycling stability of ZrCo-based alloys for hydrogen isotopes storage. *Chem. Eng. J.* **2023**, *455*, 140571. DOI
31. Bogdanović, B.; Sandrock, G. Catalyzed complex metal hydrides. *MRS. Bull.* **2002**, *27*, 712-6. DOI
32. Yao, Z.; Xiao, X.; Liang, Z.; et al. Improvement on the kinetic and thermodynamic characteristics of $Zr_{1-x}Nb_xCo$ (x = 0-0.2) alloys for hydrogen isotope storage and delivery. *J. Alloy. Compd.* **2019**, *784*, 1062-70. DOI
33. Zhou, Z.; Han, L.; Bollas, G. M. Kinetics of NiO reduction by H_2 and Ni oxidation at conditions relevant to chemical-looping combustion and reforming. *Int. J. Hydrog. Energy.* **2014**, *39*, 8535-56. DOI
34. Pielichowski, K.; Flejtuch, K. Non-oxidative thermal degradation of poly (ethylene oxide): kinetic and thermoanalytical study. *J. Anal. Appl. Pyrolysis.* **2005**, *73*, 131-8. DOI
35. Khawam, A.; Flanagan, D. R. Solid-state kinetic models: basics and mathematical fundamentals. *J. Phys. Chem. B.* **2006**, *110*, 17315-28. DOI PubMed
36. Martens, A.; Weis, P.; Krummer, M. C.; et al. Facile and systematic access to the least-coordinating WCA $[(R^FO)_3Al\text{-}F\text{-}Al(OR^F)_3]^-$ and its more lewis-basic brother $[F\text{-}Al(OR^F)_3]^-$ ($R^F = C(CF_3)_3$). *Chem. Sci.* **2018**, *9*, 7058-68. DOI
37. Yang, Z. Y.; Yuan, Y. F.; Zhu, M.; Yin, S. M.; Cheng, J. P.; Guo, S. Y. Superior rate-capability and long-lifespan carbon nanotube-in-nanotube@Sb_2S_3 anode for lithium-ion storage. *J. Mater. Chem. A.* **2021**, *9*, 22334-46. DOI
38. Han, B.; Jia, Y.; Wang, J.; et al. The structural, energetic and dehydrogenation properties of pure and Ti-doped Mg (0001) /MgH_2 (110) interfaces. *J. Mater. Chem. A.* **2023**, *11*, 26602-16. DOI
39. Wolverton, C.; Ozoliņš, V.; Asta, M. Hydrogen in aluminum: first-principles calculations of structure and thermodynamics. *Phys. Rev. B.* **2004**, 69. DOI
40. Dompablo ME, Tartaj P, Amarilla JM, Amador U. Computational investigation of Li insertion in Li_3VO_4. *Chem. Mater.* **2016**, *28*, 5643-51. DOI
41. Nagasako, N.; Fukumoto, A.; Miwa, K. First-principles calculations of C14 -type laves phase Ti-Mn hydrides. *Phys. Rev. B.* **2002**, 66. DOI
42. Sun, S.; Han, Z.; Liu, W.; et al. Lattice pinning in MoO_3 via coherent interface with stabilized Li^+ intercalation. *Nat. Commun.* **2023**, *14*, 6662. DOI PubMed PMC
43. Li, C.; Yang, W.; Liu, H.; et al. Picturing the gap between the performance and US-DOE's hydrogen storage target: a data-driven model for MgH_2 dehydrogenation. *Angew. Chem. Int. Ed. Engl.* **2024**, *63*, e202320151. DOI